Role of hydride ion within Ru/LaScSi and Ru/CeTiGe catalysts for NH3 synthesis: A combination of DFT and experimental nitrogen isotopic exchange studies

Charlotte Croisé, Khaled Alabd, Antoine Villesuzanne, Fabien Can, Xavier Courtois, Etienne Gaudin, Sophie Tencé, Nicolas Bion

Catalysis Communications 179 (2023) 106689

Contents lists available at ScienceDirect

Catalysis Communications

journal homepage: www.elsevier.com/locate/catcom

Role of hydride ion within Ru/LaScSi and Ru/CeTiGe catalysts for NH_3 synthesis: A combination of DFT and experimental nitrogen isotopic exchange studies

Charlotte Croisé [a], Khaled Alabd [b], Antoine Villesuzanne [b,*], Fabien Can [a], Xavier Courtois [a], Etienne Gaudin [b], Sophie Tencé [b], Nicolas Bion [a,*]

[a] Institut de Chimie des Milieux et Matériaux de Poitiers (IC2MP), Université de Poitiers, CNRS, F-86073 Poitiers, France
[b] Univ. Bordeaux, CNRS, Bordeaux INP, ICMCB, UMR 5026, F-33600 Pessac, France

ARTICLE INFO

Keywords:
Ammonia synthesis
Intermetallic
Ruthenium
Electride
Isotopic exchange
DFT

ABSTRACT

The design of catalysts active for ammonia synthesis under mild conditions of temperature and pressure is a new grail for its production process based on green hydrogen and intermittent renewable energy sources. Ru/LaScSi and Ru/CeTiGe are investigated with an approach combining DFT calculations and $^{15}N/^{14}N$ homomolecular exchange experiments. Ru/LaScSi is the most active of both catalysts. It has electride-like properties which are enhanced when partially hydrogenated leading to higher activity in nitrogen equilibration reaction. Ru/CeTiGe, relatively active despite the absence of electride-like character, is proposed to produce NH_3 following the associative mechanism with the assistance of absorbed H.

1. Introduction

The well-known Haber-Bosch industrial process (H-B) for ammonia production has been optimized for a century with the use of H_2 produced by steam reforming of natural gas or coal. It operates at high temperature (450–600 °C) and high pressure (150–400 bar) [1]. The economic viability of this energy-intensive process requires centralised production with a daily output of over 1000 tNH_3 [2]. The annual ammonia production by H-B process for fertilizers (~180 million tons), is consequently responsible for over 1.4% of the global CO_2 emissions and 1% of the global energy consumption [3]. In addition, new applications of this C-free molecule are planned like fuel, or as a means for long distance hydrogen transport and/or long-term storage [4]. Indeed, contrary to hydrogen, ammonia distribution benefits from worldwide shipping infrastructure and existing port facilities. Ammonia also exhibits high gravimetric (17.8 wt%) and volumetric (121 kg m^{-3}) hydrogen densities and liquefies at modest pressure (10 bar at 25 °C) or moderate temperature (−33 °C at 1 bar) [5].

One solution to reduce carbon dioxide emissions of the ammonia industry is to combine steam reforming and carbon capture and storage (CCS) technologies in the H-B process [6]. Another strategy, investigated by companies like Yara, is to feed the ammonia synthesis reactor with green H_2 [7,8]. The synthesis of ammonia with green hydrogen and for green hydrogen storage creates a new paradigm in the perception of the H-B process. The hydrogen produced by water electrolysis units using renewable energy does not necessarily require centralised large-scale plants to become economically viable. Moreover, the reduction in scale of the production mode is favourable to improve the flexibility of the process which is needed to overcome the intermittency of renewable electricity sources. However, downscaling the production unit requires the lowering of operating pressure and temperature. Indeed, capital cost will decrease by lowering the operating pressure provided that the operating temperature of this exothermic reaction is simultaneously lowered to maintain a reasonable conversion rate [9].

In 2012, Hosono et al. [10] reported the promising behaviour of an electride-type compound, identified as C12A7:e-, associated to Ru to catalyse the ammonia synthesis reaction under mild conditions of temperatures and pressures [10]. Electride-type materials have specific properties linked to the existence of zones of high electron density, as shown in particular by theoretical approaches [11]. Electrons in electride-type materials are called anionic electrons because in these solids *"the electrons detach themselves entirely from their original atoms, as with the ionic case, but do not fully transfer to a destination atom"*, as explained by Liu et al. [12] in their review article. These excess electrons

* Corresponding authors.
E-mail addresses: antoine.villesuzanne@icmcb.cnrs.fr (A. Villesuzanne), nicolas.bion@univ-poitiers.fr (N. Bion).

https://doi.org/10.1016/j.catcom.2023.106689
Received 1 March 2023; Received in revised form 3 May 2023; Accepted 4 May 2023
Available online 6 May 2023

are thus relatively free to diffuse and easily extracted which is characterized by solids with low work function. C12A7:e- is obtained by reduction of $12CaO{\cdot}7Al_2O_3$ (C12A7) removing O^{2-} from the structure in the form of molecular oxygen and leaving the excess electrons in the cages which compose the structure, thus conferring to the solid its electride-type character. The activity for the ammonia synthesis of Ru associated to this compound increases by an order of magnitude compared with benchmark Cs@Ru/MgO or Ru/active carbon catalysts. The activation energy of the reaction is greatly lowered (< 60 kJ/mol) due to the back-donation of anionic electrons to the ruthenium particles, thus weakening the N≡N bond, recognized as the rate-determining step and facilitating its cleavage. Concomitantly, the cages of the material are able to absorb H adatoms, thus limiting the poisoning of the Ru active metal surface. Since this pioneer work of Hosono et al. [13], other families of electride-type materials were developed for this reaction [13]. In particular, LaScSi compound was the first ternary intermetallic to be combined with ruthenium to synthesize NH_3 [14]. In this solid, electrons or hydrides can be located in two distinct interstitial sites of the crystal lattice: within La_4 tetrahedra and/or La_2Sc_4 octahedra cavities. A quantity of 1.5H atoms per formula unit (f.u.) can thus be stored. Combined with Ru up to 8.3 wt%, this catalyst produces 5.3 mmol g^{-1} h^{-1} at 400 °C and 1 bar, i.e. 12 times the production of the reference Ru-Cs/MgO catalyst under the same conditions [14]. LaScSi belongs to the ternary intermetallic compounds of RTX-type with R = rare earth, T = transition metal or Sc and X = p-type element. These compounds were developed for their hydrogen storage capability as the NdScSi phase, which also has two preferred interstitial sites for the insertion of 1.5H atoms per f.u. [15]. The effect on the catalytic performances of the nature of the rare earth composing these RScSi phases was recently studied [16].

A series of catalysts composed of Ru nanoparticles supported on RScSi intermetallic phases (with R = La, Ce, Pr, Nd, Sm, Gd) was evaluated. The catalytic activity of these materials followed the lanthanide series with a decrease from La to Gd and seemed to be correlated to the formation of the hydride phase. Cerium-based intermetallic compound (Ru/CeScSi) showed remarkable catalytic activity under mild conditions (0.58 mmol g^{-1} h^{-1} at 300 °C and 1 bar) associated with reversible hydrogen storage/release properties. This previous work suggested that the electride-type materials' character and thus the electron donor effect could be tuned through partial hydrogenation of the intermetallic phase. Over LaRuSi which is also identified as an electride-type compound, Brix et al. [17] reported in a DFT study that the bulk electride-type materials' character disappeared when the bulk $[La]_4$ cavities were occupied by hydrogen atoms, and suggested that the bulk electride-type materials' character did not impact the catalytic properties of the surface [17].

The aim of the present study is to better evidence the correlation between the electride-type materials' character, the partial hydrogenation of RTX-type structure, and the capacity of these compounds for dissociative activation of N_2. Two compositions of LaScSi and CeTiGe were investigated based on $^{15}N_2/^{14}N_2$ isotopic homomolecular exchange and theoretical calculations. The compositions were chosen based on preliminary calculations showing a gap in the electride-type material's character between both selected materials.

2. Experimental

2.1. Materials

The intermetallic LaScSi and CeTiGe samples were synthesized from melting the pure elements, starting from rare earth ingots (La 99.9% Sigma-Aldrich, Ce 99.8% Alfa Aesar), Sc pieces (99.9% Neyco), Ti pieces (pure, at least 99.9%, J. Morita,) and Ge lumps (99.999% Alfa Aesar). Rare earth metals and Ti pieces were pre-melted in a high-frequency furnace to evaporate volatile oxides. The molar ratio of 1:1.05:1 with an excess of scandium was used for the synthesis of LaScSi sample to compensate for residual ScO present in the Sc precursor. The CeTiGe sample was synthesized using the molar 32.5: 34.5: 33.0 ratio to minimize the presence of secondary phases. The elements were arc-melted together five times under a pure Ar gas atmosphere (≈700 mbar), returning the button upside down in between each melting to ensure homogeneity. The weight loss of the resulting silvery buttons of about 5 g was <0.3 wt% after melting. The resulting melted buttons were later wrapped in tantalum foil, sealed in a primary evacuated quartz ampoule, and annealed at 900 °C for 4 weeks. The powder of CeTiGe obtained after crushing of the CeTiGe button was cold-pressed into a pellet and annealed at 1100 °C for 3 days to obtain the high temperature form (which crystallizes with the CeScSi-type structure [15]). At the end of annealing, the sample was quenched to room temperature. Refinement of the Powder X-Ray Diffraction (PXRD) pattern shows almost equal amounts of the high-temperature (HT) and low-temperature (LT) forms of CeTiGe, as expected according to previous work [18].

Hydrogenation of LaScSi was carried out ex-situ inside a stainless-steel hydrogen autoclave. The fresh hand-milled powdered sample was placed inside a quartz tube first and then placed inside the hydrogen autoclave. The autoclave was sealed using a graphite gasket, then evacuated and rinsed with argon three times. The temperature was then elevated to 250 °C under a dynamic vacuum and held there for two hours to reach an activated state. After activation, the temperature was raised again slowly to 350 °C. Hydrogen gas was introduced quickly to the chamber after the stabilization of the temperature, hydrogenation took place under a static gauge pressure of 5 bar for 20 h. The corresponding hydrogenated LaScSi will be hereafter denoted as $LaScSiH_{1.5}$.

The deposition of Ru was made on the LaScSi, $LaScSiH_{1.5}$ and CeTiGe solids intermetallic materials previously sieved in the range 40–100 μm, by following the same protocol used in [10]. A theoretical amount of 2.5 wt% Ru was used for chemical vapor deposition using $Ru_3(CO)_{12}$ as Ru precursor in an evacuated quartz tube at 250 °C. The corresponding catalysts are hereafter denoted as Ru/LaScSi, Ru/$LaScSiH_{1.5}$ and Ru/CeTiGe samples.

2.2. Catalyst characterization

The Ru loading was determined by inductively coupled plasma optical emission spectrometry (ICP-OES), using a mixture of HNO_3 and HCl and microwaves activation to dissolve the sample. The analysis was performed in an Agilent 5110S instrument.

The crystallographic structure of the samples were analyzed before and after isotopic exchange by PXRD. The data were collected on a D8 ADVANCE Bruker AXS diffractometer in Bragg-Brentano setup equipped with a copper anode source (λ = 1.5418 Å), and a linear detector LYNXEYE XE-T. The measurements were performed at room temperature over an angular range: 8° < 2θ < 80° with a step of 0.02° and an acquisition time of 1 s per step. PXRD patterns were analyzed using the Fullprof Suite program and the unit cell parameters were determined through full-pattern matching [19].

Transmission Electron Microscopy (TEM) was performed in a JEOL 2100 UHR apparatus, equipped with a LaB_6 filament and a Gatan Ultra scan camera. The equipment uses the range of 0–20 keV of X-rays from the sample to electron impact. EDX spectroscopy was carried out with a Hypernine (Premium) detector (active area: 30 mm^2) using the software SM-JED 2300 T for data acquisition and treatment.

The thermal stability of hydrides contained in the interstitial sites of Ru/LaScSi and Ru/CeTiGe intermetallic phases were evaluated by temperature-programmed desorption (TPD) under 30 mL min^{-1} of Ar flow from RT to 1000 °C (heating ramp rate of 5 °C min^{-1}). The measurements were performed on a Micromeritics Autochem 2920 apparatus equipped with a thermal conductivity detector (TCD) to monitor the H_2 release resulting from the hydride desorption. 50 mg of sample was placed in a U-shape quartz reactor. Before the measurement, catalysts were first treated under pure hydrogen from RT to 350 °C (5 °C min^{-1}) and cooled down to RT under H_2, followed by a purge under Ar for 1 h.

2.3. Nitrogen isotopic exchange

Nitrogen isotopic homomolecular exchange (NIHE) reaction study (also called equilibration reaction), in which a mixture of $^{15}N_2$ (170 mbar) and $^{14}N_2$ (170 mbar) is scrambled over the Ru/intermetallic surface, was performed at 500 °C in a closed recycling system (70 cm^3) connected to a mass spectrometer (Pfeiffer Vacuum) on one side and to a vacuum pump on the other side. This set-up was described in a previous work dealing with oxygen isotopic exchange studies [20]. Before each analysis, the samples (60 mg), introduced in a U-shape reactor of 9.6 cm^3 were pretreated to preserve the total hydrogenation or to obtain a partially hydrogenated material. Details of the pretreatment are given later. Then, the system was outgassed using primary vacuum and the isotopic gas mixture charged. The mass numbers, $m/z = 28, 29, 30$ were continuously monitored as a function of time to follow the isotopes exchange. The m/z of 2, 17 and 18 were also recorded to determine if H atoms remained at the surface of the solid, thus yielding NH_3 or H_2 in the gas phase after reaction or simple decomposition. The presence of NO_x and O_2 was also checked by monitoring the corresponding m/z values. The equations to calculate the nitrogen equilibration reaction rate were adapted from those previously detailed in [21] for $^{18}O/^{16}O$ homomolecular exchange. Typically, the initial rate of equilibration, R_q, is given by Eq. (1), where N_g is the number of ^{15}N and ^{14}N in the gas phase, P_0 the total pressure, P_{29} the partial pressure of $^{14}N^{15}N$ and t the time of equilibration reaction (t being limited to 10 or 40 min of reaction for the calculation depending on the sample).

$$R_q = \frac{2N_g}{P_0}\left(\frac{dP_{29}}{dt}\right) \quad (1)$$

2.4. Catalytic ammonia synthesis

The catalytic tests were carried out in a fixed-bed quartz reactor inserted in a stainless- steel reactor enabling measurements until 5 bar pressure. 100-mg catalyst sample in powder form was used and the reactant gas mixture was composed of a flow of H_2:N_2 = 3:1 (purity of N_2 > 99.9999% and H_2 > 99.9999%). The total volume flow rate was fixed at 60 mL min^{-1}. The compositions of the feed gas and effluent stream were monitored continuously (1 Hz) using online gas analysis (MKS 2030 Multigas infrared analyzer) with high NH_3 sensitivity (2–3 ppm). Ammonia production was measured in isothermal conditions at 400 °C and 1, 3 and 5 bar consecutively, after heating under reactant gas mixture from RT with an intermediate 1 h-step at 300 °C (heating ramp rate of 5 °C min^{-1}). Results are expressed directly in terms of emitted ammonia (ppm) or production rate (mmol h^{-1} g^{-1}).

2.5. DFT calculations

Spin-polarized electronic structure calculations were achieved using density functional theory (DFT) with the projector augmented-wave (PAW) method as implemented in the VASP code [22–24]. PAW datasets were used to describe valence electron-ionic core interactions. For the relaxation of cell parameters and atomic positions of CeTiGeH, the exchange and correlation energies were treated at the generalized gradient approximation (GGA) level, according to the Perdew-Burke-Ernzerhof formulation [25]; an on-site Hubbard correction U of 5 eV [26–29] was added to Ce 4f orbitals, according to Dudarev's scheme [30]. For the density of states and electron density distribution, we used the more accurate Heyd-Scuseria-Ernzerhof (HSE06) screened hybrid exchange functional, where 25% of GGA exchange is replaced by exact Hartree-Fock (HF) exchange [31,32]. The HSE06 scheme is much more demanding than GGA in terms of computational resources but is expected to improve significantly the accuracy of the calculated energy spectrum (density of states). Γ-centered Brillouin zone samplings of 16 × 16 × 4 and 8 × 8 × 2 k-points were used for GGA + U and HSE06 calculations, respectively. The plane-wave energy cutoff was 250 eV and 310 eV for LaScSi(H) and CeTiGe(H), respectively. Partial band occupancies were treated by the tetrahedron method with Blöchl corrections, or by Gaussian smearing, with a width of 0.05 eV. The self-consistency criteria were 10^{-3} eV per cell for electronic convergence, and 10^{-2} eV/Å for forces in structural optimizations. R.F.W. Bader's Quantum Theory of Atoms in Molecules (QTAIM) [33], as implemented in the Bader Charge Analysis code [34], was used to partition the valence electron density and further integrate it in atomic basins, to reach atomic charges. The QTAIM method fully partitions the electron density into atomic basins, giving rise to atomic charges and to a non-ambiguous identification for non-nuclear maxima; as such, it has been widely used to identify and characterize electrides-type materials [35–42]. Isovalues of the electron density were visualized using VESTA [43].

All calculations were done using the Z = 2 tetragonal unit cells (Fig. 1), with experimental crystal structures as input for LaScSi [44] and CeTiGe [18]. For LaScSiH, we used the experimental cell parameters and the atomic positions for LaScSi (i.e., z coordinate for La and Si). For LaScSiH, we used the experimental cell parameters [45] and the atomic positions for LaScSi (i.e., z coordinate for La and Si). For CeTiGeH, the cell parameters and z parameters of Ce and Ge were relaxed within DFT/GGA + U under space group I4/mmm; as expected, an increase of c parameter and a decrease of a cell parameter were obtained upon hydrogen insertion (a = 4.088 Å; c = 18.219 Å; z(Ce) = 0.3225; z(Ge) = 0.0969). Note that, in our previous work on intermetallic compounds with a similar crystal structure, the atomic positions and cell parameters optimized within both GGA + U and HSE06 schemes were close to experimental values [46]. Therefore, no residual strains of a magnitude that could affect our conclusions (all of qualitative nature) are expected in the present study.

3. Results and discussion

3.1. Catalytic ammonia synthesis

The deposition of Ru obtained by chemical vapor deposition in an evacuated and sealed quartz tube containing the powder of intermetallic material does not permit a perfect control of the amount of Ru really impregnated on the RTX phase. However, the very low porosity of these solids and their sensitivity in aqueous phase hinder the utilization of classical dry and wet impregnation of Ru precursor. It results in a difficulty to maintain constant the content of Ru for all the studied catalysts (Table 1). Both Ru/LaScSi$H_{1.5}$ and Ru/CeTiGe samples contain 1.9 wt% Ru, while the non-hydrogenated Ru/LaScSi contains 3 wt% Ru. The morphology of the Ru particles is also very heterogeneous (Fig. 2). Some pseudo spherical particles with 4–12 nm size are visible on the TEM pictures for all the catalysts. Other rod-shaped particles are also present on non-hydrogenated Ru/LaScSi and Ru/CeTiGe solids with dimensions in the range of 25 to 40 nm in length, and 3 to 5 nm in width. Because of the absence of homogeneity in the particles morphology, it is quite complex to present any histogram of the Ru size distribution.

The performances in ammonia synthesis were compared amongst Ru/LaScSi, Ru/LaScSi$H_{1.5}$ and Ru/CeTiGe catalysts at 400 °C under a reaction mixture composed of N_2:H_2 = 1:3 (total flowrate = 60 mL min^{-1}) and at 1, 3 and 5 bar. The outlet ammonia concentrations are presented in Table 1 for the different pressures, and a comparison is presented in Fig. 3 in terms of rate of ammonia produced per gram of sample after 1 h of time-on-stream. As reported in a previous work [16], Ru/LaScSi is active at 400 °C with a production rate of 1.37 mmol NH_3 h^{-1} g^{-1} at 1 bar. The ammonia is slightly lower for the Ru/LaScSi$H_{1.5}$ (0.85 mmol h^{-1} g^{-1}) which is explained by the lower loading of Ru (1.9 wt% compared to 3 wt%, respectively). Indeed, the ratio of the ammonia rates obtained for the two catalysts is the same as the ratio of Ru loadings. Ru/CeTiGe, which was never tested for ammonia synthesis reaction, shows relatively good performances at 400 °C with 0.75 mmol h^{-1} g^{-1} but below that of LaScSi support. This difference could also be due to a difference in the Ru accessibility originated from the largest particles

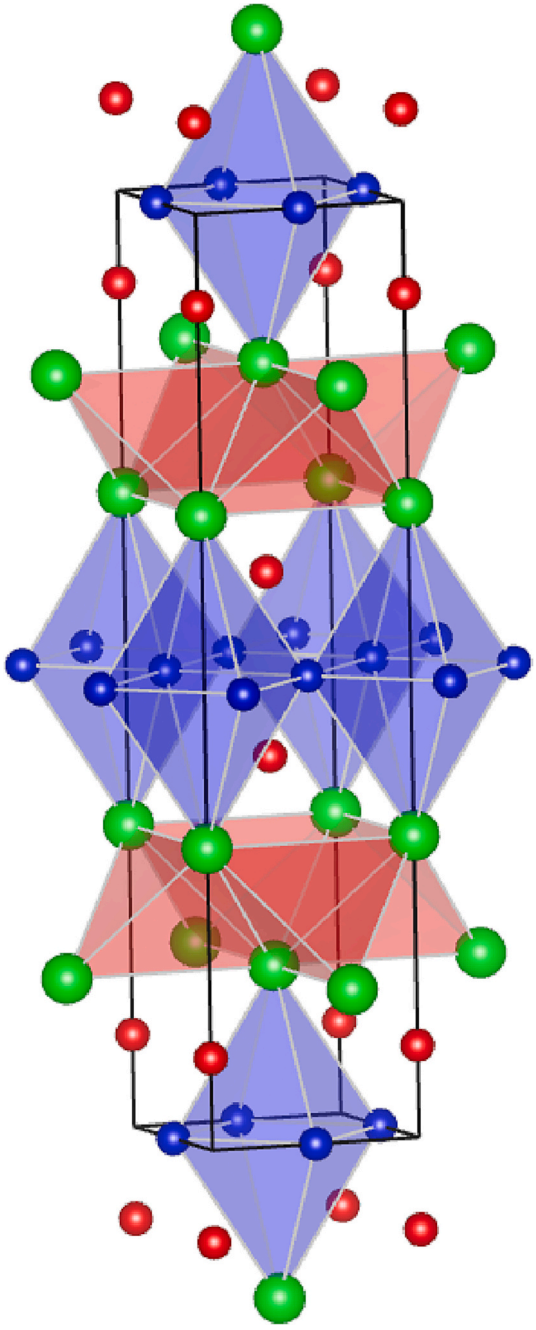

Fig. 1. Schematic representation of the crystal structure of LaScSi and CeTiGe. Green spheres: La (resp. Ce). Blue spheres: Sc (Resp Ti). Red spheres: Si (resp. Ge). The Z = 2 unit cell is represented, as well as vacant octahedral and tetrahedral sites. In LaScSiH and CeTiGeH, hydride ions are located in the tetrahedral sites of the rare earth double layers. (For interpretation of the references to colour in this figure legend, the reader is referred to the web version of this article.)

Table 1
Ruthenium loadings and outlet NH_3 concentrations recorded at various pressures and 400 °C over the different Ru/RTX catalysts.

Catalyst	Metal content (%)	NH_3 concentration (ppm)		
		1 bar	3 bar	5 bar
Ru/LaScSi	3.0	912	2114	3556
Ru/LaScSiH$_{1.5}$	1.9	568	1375	3000
Ru/CeTiGe	1.9	500	935	1290
Ru/CeTiGe (IE)	2.4			

detected for Ru/CeTiGe. As expected, the ammonia yield increases with the pressure from 1 to 5 bar. Almost the same differences in activity are observed for all the pressures between hydrogenated and non-hydrogenated Ru/LaScSiH$_{1.5}$. On the contrary, the activity gap increases between Ru/CeTiGe and Ru/LaScSiH$_{1.5}$ with increasing the pressure. At 5 bar, the ammonia rate is 4.49 mmol h^{-1} g^{-1} for Ru/LaScSiH$_{1.5}$ versus 1.93 mmol h^{-1} g^{-1} for Ru/CeTiGe. Finally, the pressure was decreased to 1 bar at the end of the test to detect a possible deactivation. Compared to the first measurement at 1 bar, a lower ammonia rate is observed for the three samples but with different amplitudes corresponding to an activity loss of 6, 5 and 20% for Ru/LaScSiH$_{1.5}$, Ru/LaScSiH$_{1.5}$ and Ru/CeTiGe, respectively.

3.2. *Stability of the RTXH hydrides*

TPD experiments under the flow of Ar were carried out from RT to 1000 °C. For Ru/LaScSi and Ru/CeTiGe which were not previously ex-situ hydrogenated (see experimental part), an in situ hydrogenation was used under pure H_2 flow at 350 °C for 1 h followed by a purge with Ar at RT for 30 min. For Ru/LaScSiH$_{1.5}$ a simple purge under Ar at RT was used before TPD. The TPD profiles are presented for the three samples in Fig. 4. The curve corresponding to Ru/LaScSi exhibits two maxima at 519 and 613 °C. The first peak seems to be narrow, while the second one is very wide. It is in good agreement with the temperatures of desorption at 525 and 625 °C reported for LaScSi in a previous study [16]. Based on the relative ratio of areas between the two peaks, the first peak is assigned to the desorption of the hydride ions from the octahedral La_2Sc_4 cavities first, and the second one, at higher temperatures, is attributed to the desorption from the La_4 tetrahedral cavities. Also, according to Wu et al. [14] *h*ydrides stored in the tetrahedral site are supposed to be more thermally stable. The profile of H_2 desorption for Ru/LaScSiH$_{1.5}$ varies with one single wide peak centred at 583 °C (red curve). However, this large peak can reasonably include the two previous narrow and wide described peaks corresponding to the desorption from octahedral and tetrahedral cavities, respectively. The difference of profile could be due to the difference of hydrogenation protocol; a higher desorption temperature of the hydrides inserted inside the octahedral cavities would be obtained when hydrogenation is performed in static conditions under 5 bar of H_2 during 20 h. Consequently, the narrow peak would be shifted to higher temperatures compared with the Ru/LaScSi, leading to a strong overlap of the two peaks. Finally, the profile of CeTiGe appears different with a slow and monotone desorption of H_2 between 300 and 500 °C followed by a faster desorption above 500 °C which is illustrated by a peak centred at 609 °C. It has been shown in a previous work that CeTiGe can absorb 1.5 atoms of H f.u.$^{-1}$, based on neutron diffraction studies, confirming the localisation of H atoms in the Ce_4 tetrahedra and the Ti_4Ce_2 octahedral sites [47]. By analogy with LaScSi, one can suspect that the peak at higher temperatures would be characteristic of the desorption of hydride ions from Ce_4 tetrahedral cavities, but further studies are required for a more precise assignment. Anyway, these first results demonstrate the different behaviour of these materials. Moreover, these results also show, in agreement with the work already reported [16], that the pre-treatment under hydrogen at 350 °C is sufficient to hydrogenate the intermetallic phase.

3.3. $^{15}N_2/^{14}N_2$ *homomolecular exchange reaction*

Nitrogen isotopic homomolecular exchange (NIHE) reaction, $^{14}N_2 + {}^{15}N_2 \leftrightharpoons 2\ {}^{14}N^{15}N$, was historically used on catalytic systems of interest for ammonia synthesis, most notably those based on Ru [48,49]. Indeed, the isotopic equilibration reaction is representative of the N≡N bond cleavage, and the N_2 dissociation is usually reported as the rate-limiting step in the ammonia synthesis reaction. It might be then anticipated that the rate of NIHE reaction could be correlated to NH_3 synthesis activity. Accordingly, NIHE experiments were carried out aiming at comparing

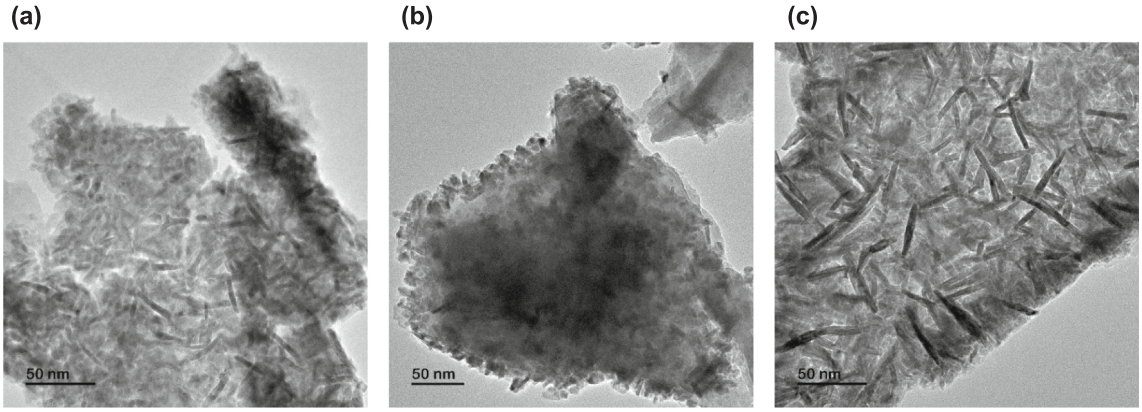

Fig. 2. TEM pictures of (a) Ru/LaScSi, (b) Ru/LaScSiH$_{1.5}$ and (c) Ru/CeTiGe solids.

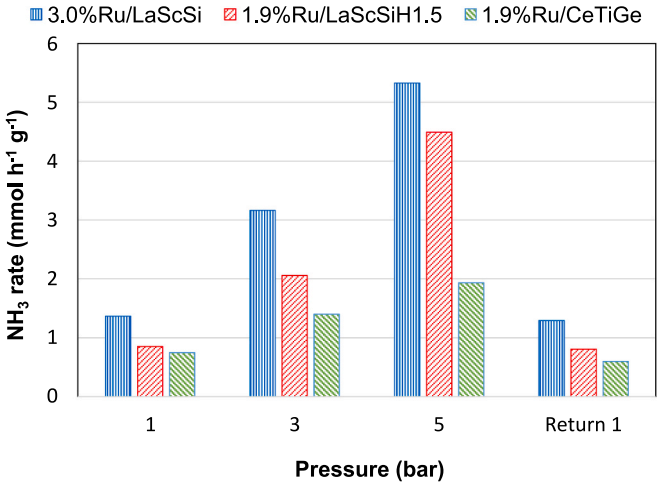

Fig. 3. Production of NH_3 over Ru/Intermetallic catalysts at 400 °C and various pressures.

the behaviour of LaScSi and CeTiGe solids. A systematic study was already reported in a previous work showing that LaScSi was active at 450 °C for the isotopic equilibration reaction [16]. A comparison of the effect of *R* element in a series of $Ru_{1.7}/RScSi$ intermetallic phases (with R = La, Ce, Pr, Nd, Sm, Gd) in both NH_3 synthesis and $^{15}N/^{14}N$ exchange confirmed the interrelationship between the two reaction rates. However, the study did not allow to control the hydrogenation of the intermetallic materials during the exchange. Moreover, CeTiGe was not tested in this previous work.

Fig. 4 shows the nitrogen isotopic distribution obtained over Ru/LaScSiH$_{1.5}$ during NIHE reaction at 500 °C. The experiments illustrated in Fig. 5a and Fig. 5b differ according to the treatment that was used before the nitrogen equilibration reaction. For the two experiments, a treatment under pure H_2 flow was done to ensure the metallic state of Ru. Then, a first experiment aimed at preserving the complete hydrogenation of the sample by heating the material under primary vacuum at 500 °C before introduction of the 340-mbar nitrogen isotope gas mixture. At this temperature, the primary vacuum is supposed to preserve the hydrides in the interstitial sites of LaScSi material. The corresponding experiment is presented in Fig. 5a. The nitrogen equilibration rate R_q is quite low with 4.0×10^{22} at. N min^{-1} g^{-1}, and a production of 27.5 mbar of $^{14}N^{15}N$ after 3 h of reaction. A small release of H_2 is observed after introduction of the nitrogen mixture indicating the presence of unstable H in the material. In a second experiment, presented in Fig. 5b, the Ru/LaScSiH$_{1.5}$ catalyst was flushed with pure Ar from 250 to 500 °C and maintained at 500 °C for 2 h under Ar flow.

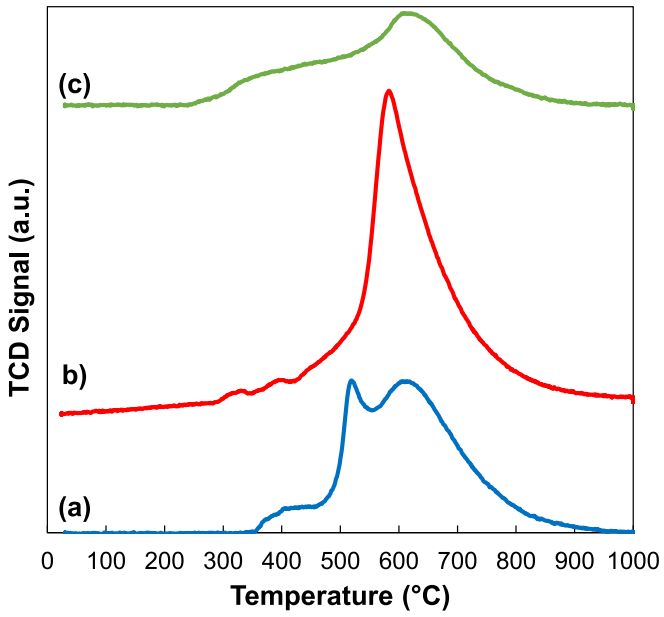

Fig. 4. TPD under Ar gas flow of a) Ru/LaScSi, (b) Ru/LaScSiH$_{1.5}$ and (c) Ru/CeTiGe. For Ru/LaScSi and Ru/CeTiGe, TPD followed an hydrogenation step at 350 °C under pure H_2 for 1 h; for Ru/LaScSiH$_{1.5}$, the pre-treatment was limited to an Ar gas purge at RT for 30 min.

According to the TPD analysis, a partial removal of the hydride species is expected with this treatment. Indeed, the desorption of H_2 from Ru/LaScSiH$_{1.5}$ was detected above 450 °C (Fig. 4, red curve b). The material subjected to this treatment is denoted hereafter as Ru/LaScSiH$_x$. The result of this experiment, reported in Fig. 5b, shows that such a treatment promotes the equilibration rate, with a Rq value of 14.5×10^{22} at. N min^{-1} g^{-1} and a partial pressure of $^{14}N^{15}N$, which reaches 115 mbar after 3 h.

PXRD analysis was used to evaluate the hydrogenation state of the Ru/LaScSiH$_x$ sample recovered after the isotopic exchange experiment presented in Fig. 5b. Fig. 6 shows the corresponding PXRD pattern in the 2θ range of 25 to 40° with cell parameters given in Table 2. The sample Ru/LaScSiH$_{1.5}$ before the isotopic exchange was included as a reference. The PXRD pattern shows a slight degradation of the sample. The main phase is a partial hydride LaScSiH$_{x1}$ with estimated cell parameters of a = 4.28 Å and c = 16.6 Å. The significant broadening of the peaks, as seen in the (006) reflection results from micro-strain and inhomogeneity of the cell parameters, especially for the c parameter. However, we can confidently conclude that such hydrides are intermediates between

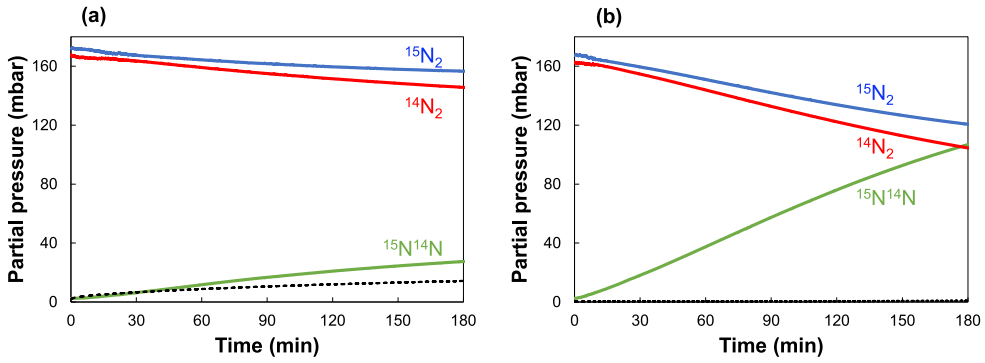

Fig. 5. Nitrogen isotopic distribution during $^{15}N_2/^{14}N_2$ homomolecular exchange at 500 °C over (a) Ru/LaScSiH$_{1.5}$ and (b) Ru/LaScSiH$_{1.5}$ partially dehydrogenated (hereafter denoted as Ru/LaScSiH$_x$) after 2 h treatment under Ar flow at 500 °C (dashed line represents the evolution of the partial pressure of H_2 from signal $m/z = 2$).

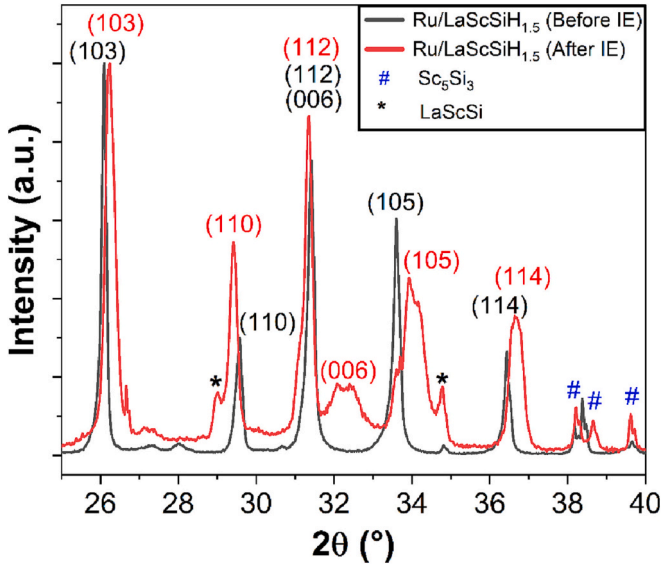

Fig. 6. PXRD patterns of LaScSiH$_{1.5}$ before isotopic exchange (black) and LaScSiH$_x$ after the isotopic exchange corresponding to the Fig. 5b (red). The (hkl) indices given in black and red corresponds to the LaScSiH$_{1.5}$ and LaScSiH$_{x1}$ phases, respectively (see Table 2 for cell parameters). (For interpretation of the references to colour in this figure legend, the reader is referred to the web version of this article.)

Table 2
Cell parameters of the phase found after isotopic exchange and the corresponding references RTX and RTXH$_{1.5}$.

Composition	a (Å)	c (Å)	Ref
LaScSi	4.355	16.031	[16]
LaScSiH$_{1.5}$	4.271	17.090	[14]
LaScSiH$_{x1}$	4.28	16.6	This study
CeTiGe (HT)	4.15447	15.8814	[47]
CeTiGeH$_{1.5}$	4.0889	16.9917	[47]
CeTiGeH$_{x1}$	4.13	16.1	This study
CeTiGeH$_{x2}$	4.10	17.4	This study

LaScSi and LaScSiH$_{1.5}$. The pattern also shows that a part of the LaScSi intermetallic exists as a secondary phase.

Similar nitrogen exchange experiments were carried out over the Ru/CeTiGe catalyst. Note that a new batch of sample was necessary for these measurements with a slightly superior Ru loading (2.4 wt%, see Table 1). In the absence of ex-situ hydrogenated material before the nitrogen exchange experiment, a specific protocol was used based on the TPD analysis. Indeed, the H_2-TPD profile obtained with Ru/CeTiGe suggested that a treatment under pure H_2 at 350 °C for 1 h at atmospheric pressure was sufficient for a complete hydrogenation of the sample, as previously discussed in Section 3.2. This treatment was used in situ in the isotopic exchange set-up followed by a heating under primary vacuum until 500 °C before introducing the $^{14}N_2 + {}^{15}N_2$ equimolar gas mixture. No equilibration activity was then observed. Different protocols were successively applied to partially dehydrogenate the sample. Each time, the nitrogen isotopic distribution monitored during the NIHE reaction demonstrated the absence of activity (Fig. 7).

Fig. 8 shows the PXRD pattern of the pristine CeTiGe sample (black) where the indexation marks the peaks of the high-temperature form, while the green marker shows the main peak of the low-temperature form of CeTiGe. After the nitrogen isotopic exchange experiment, the partially hydrogenated Ru/CeTiGeH$_x$ (in red) sample suffered a decomposition. However, the main phase obtained CeTiGeH$_{x1}$ is an hydride with cell parameters closer to CeTiGe than to CeTiGeH$_{1.5}$. It should be noted that this sample also had small amounts of CeTiGeH$_{x2}$ with the cell parameters close to those of CeTiGeH$_{1.5}$ (Table 2).

3.4. DFT calculations

3.4.1. LaScSi versus CeTiGe solids

Fig. 9 shows the density of states for LaScSi and CeTiGe, calculated within DFT/HSE06. As expected, LaScSi is found non-magnetic, whereas CeTiGe shows a pronounced spin polarization (ferromagnetic state) of

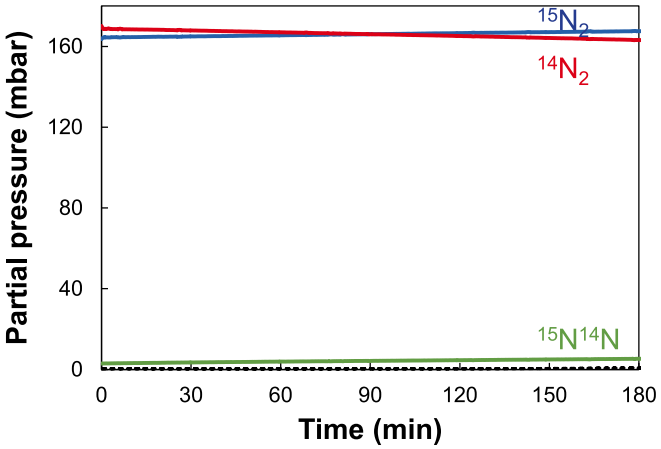

Fig. 7. Nitrogen isotopic distribution during $^{15}N_2/^{14}N_2$ homomolecular exchange at 500 °C over Ru/CeTiGe partially hydrogenated hereafter denoted as Ru/CeTiGe$_x$ (dashed line represents the evolution of the partial pressure of H_2 from signal $m/z = 2$).

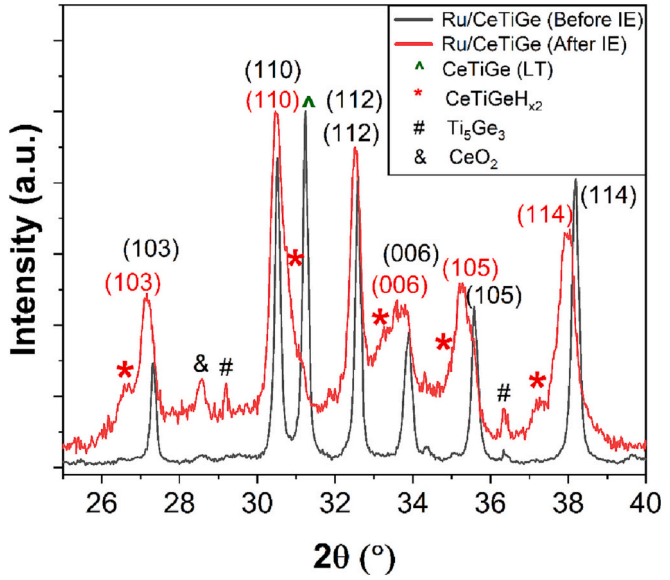

Fig. 8. PXRD pattern of pristine CeTiGe (black) and partially hydrogenated $CeTiGeH_x$ (red) after isotopic exchange. The (hkl) indices given in black and red corresponds to the HT-CeTiGe and $CeTiGeH_{x1}$ phase, respectively (see Table 2 for cell parameters). (For interpretation of the references to colour in this figure legend, the reader is referred to the web version of this article.)

Ce 4f and 5d bands, and of Ti 3d bands. The magnetic moment found for CeTiGe is close to 3 μ_B per f.u., with similar contributions from Ce 4f and Ti 3d shells, and to a lesser extent from the Ce 5d bands. The 3d electron populations for Sc and Ti correspond to configurations $3d^1$ and $3d^2$, respectively. The electride-type material's character of the two compounds was assessed by i) partitioning the electron density according to the QTAIM scheme, and ii) examining the electron density distribution in the vacant R_2T_4 octahedral sites (R = La, Ce; T = Sc, Ti, Fig. 1). Table 3 lists the QTAIM valence electron populations found in atomic basins. The whole electron density could be partitioned unambiguously from the QTAIM method, as checked from the sum of electron populations from all identified basins. A common feature of QTAIM charges is that they slightly differ from the ones derived from Mulliken charges or cumulated partial density of states. Here, a maximum in electron density (pseudo-atom) is clearly found in LaScSi, in agreement with similar studies reported [14,50]; no such feature was identified in CeTiGe. Also, no electride-type charge density was found in tetrahedral sites of the rare earth double layers (Fig. 1), contrary to what was claimed in the literature [14].

The respective electride- vs. non-electride-type characters of LaScSi and CeTiGe are also illustrated by isovalues of the valence electron density in the R_2T_4 octahedral sites (R = La, Ce; T = Sc, Ti) as shown in Fig. 10. A cushion-like, pseudo-atomic electron density is clearly identified in the vacant octahedral site in LaScSi, nothing such in CeTiGe.

This striking difference between the two compounds is consistent with our studies (to be published) on intermetallic systems with the same crystal structure and either Sc or Ti as transition element: RScX compounds show clear electride-type features, but RTiX do not. This is in agreement with DFT high-throughput screening of materials databases, which identified Sc-derived intermetallic compounds in this structural family as electride-type materials, but no candidates were found in Ti-derived compounds [37]. As suggested by Hosono et al. [14], the electride-type charge density in the R_2Sc_4 sites may arise from the overlap of 4 s/4p Sc orbitals; if this is the case, then the radial extension of Ti 4 s and 4p orbitals could not match across the octahedral site to generate a local maximum of electron density. The electride-type materials features may also be prohibited in Ti-derived intermetallics of this series due to the spin-polarization of Ti-character bands: majority- and

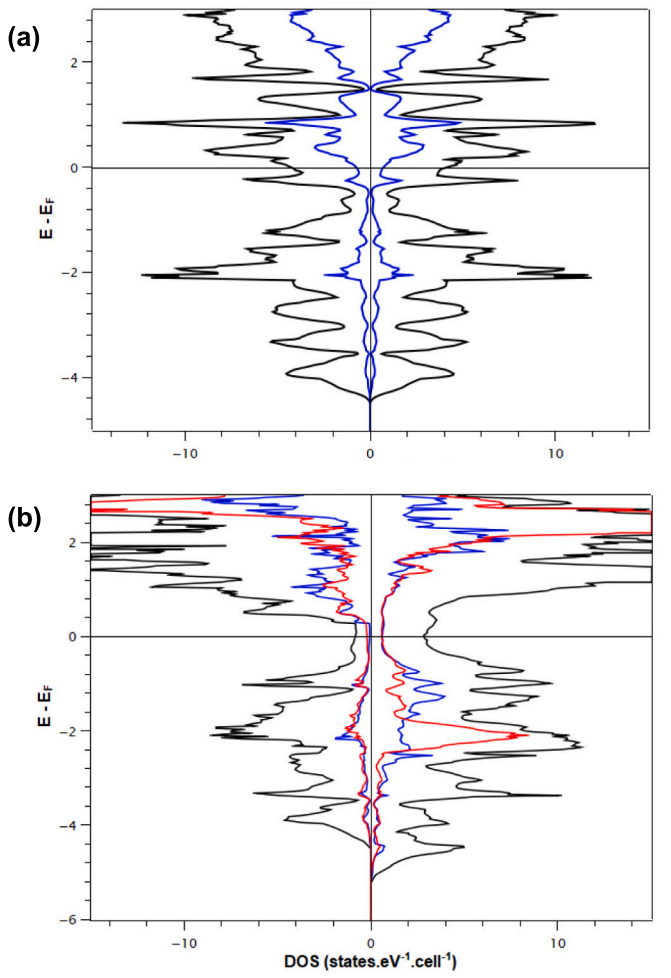

Fig. 9. Density of states (DOS) for (a) LaScSi (top) and (b) CeTiGe, from DFT/HSE06 hybrid calculations. Blue line: Sc and Ti partial DOS. Red line: Ce partial DOS. Minority and majority spin channels are on the left and right sides, respectively. (For interpretation of the references to colour in this figure legend, the reader is referred to the web version of this article.)

Table 3
Electron populations in atomic basins in LaScSi and CeTiGe, from QTAIM partitioning of the valence electron density. The vacancy is located in the R_2T_4 octahedral site (R = La, Ce; T = Sc, Ti). Note that the sum of QTAIM populations amounts to the total number of valence electrons per formula unit (2 vacancies per f.u.)

	La/Ce	Sc/Ti	Si/Ge	Vacancy	Total
LaScSi	9.87	0.88	6.71	1.08	18.00
CeTiGe	10.85	2.87	6.28	0.00	20.00

minority-spin spin channels have, in essence, different electronic structures and thus differences in chemical bonding as well.

3.4.2. *LaScSiH vs. CeTiGeH*

One hydrogen atom per f.u. corresponds to the full occupation of the tetrahedral sites in the rare earth double layers. DOS curves in Fig. 11 show a gap opening in LaScSi upon hydrogen insertion, with still a non-magnetic electronic structure. The main significant change in the DOS curves of CeTiGeH, with respect to CeTiGe is a spontaneous antiferromagnetic ordering of Ce 4f and Ti 3d orbitals, whereas CeTiGe appeared as ferromagnetic. This was confirmed by performing another calculation starting from an antiferromagnetic arrangement for atomic moments, leading to an identical electronic structure after self-consistency was

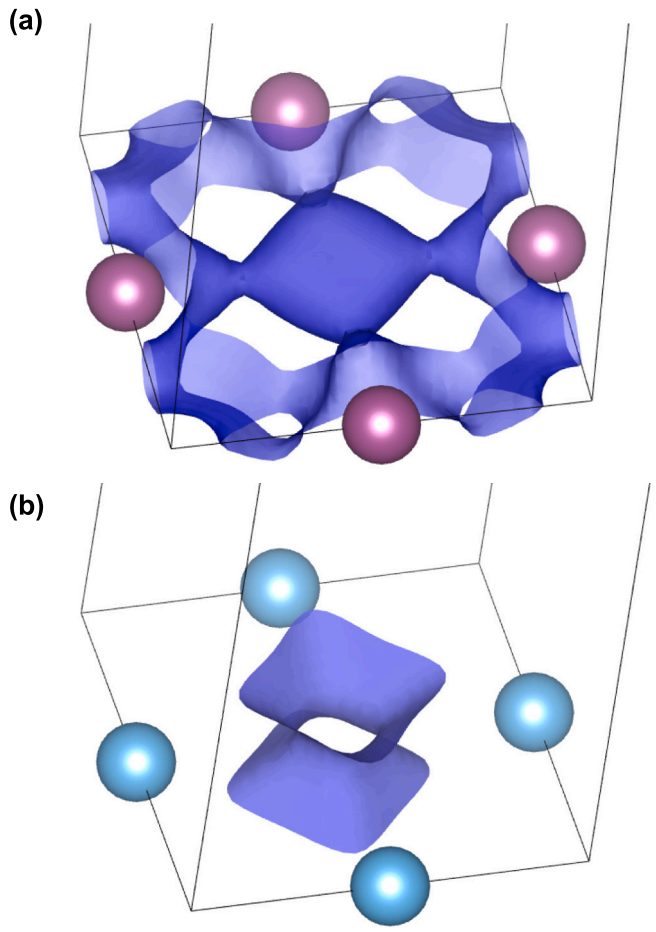

Fig. 10. Isovalue ($\rho = 2.0 \times 10^{-2}$ e$^-$.Å^{-3}) plots of the electron density in the Sc and Ti layers of (a) LaScSi and (b) CeTiGe based on DFT/HSE06 hybrid calculations.

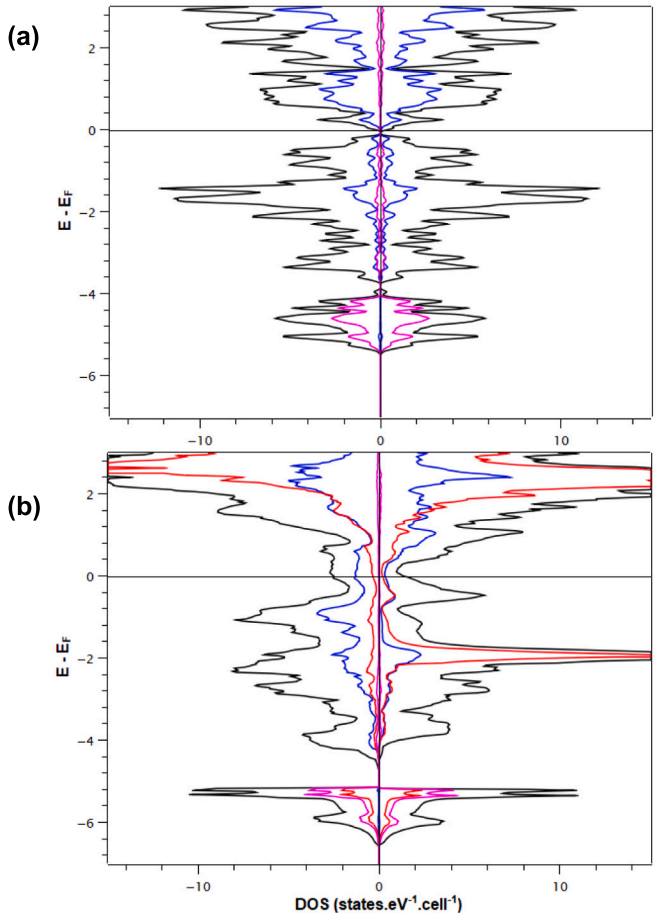

Fig. 11. Density of states (DOS) for (a) LaScSiH and (b) CeTiGeH based on DFT/HSE06 hybrid calculations. Partial DOS for Sc and Ti (blue), Ce (red) and H (pink) are represented. Minority and majority spin channels are on the left and right sides, respectively. (For interpretation of the references to colour in this figure legend, the reader is referred to the web version of this article.)

achieved.

Hydrogen bands are located at lower energies than the pristine valence bands, corresponding to hydride ions H^-, and involving large R-H covalent interactions, as revealed by the partial DOS curves and the significant band width. The profound effects of R-H covalent interactions were discussed in our previous works on GdScGe, NdScSi, $NdScSiC_{0.5}$ and their hydrides [46,51]. Otherwise, the insertion of hydrogen ions in tetrahedral sites does not affect the (non-)electride-type character in both compounds, as seen from Fig. 12 and Table 4, at least from the point of view of the electron density distribution. Nevertheless, an important effect of hydrogen insertion is the lowering of the Fermi level, which could depopulate electride-type materials states. Fig. 12 and Table 4 show that the electride-type materials character is fully preserved in LaScSi upon hydrogen intake, at least up to one hydrogen atom per formula unit. Naturally then, hydrogen insertion could bring electride-type materials states closer to Fermi level (due to the lowering of the latter), and thus reinforce it or at least make it more efficient as electron reservoir. For example, electride-type electrons lie within 0.1 eV below Fermi level in GdScGe [46], and we identified electride-type materials states in LaScSi in the range of 0.5–1 eV below Fermi level, alike what was found from DFT + DMFT studies [50]. This is probably also why LaScSi was not identified as electride-type material in [37], since the search for electride-type material properties was restricted to an energy range of 0.2 eV below Fermi level. Note that beyond one hydrogen atom per formula unit, hydrogen atoms start to take place in octahedral sites, progressively cancelling electride-type material characteristics in $LaScSiH_x$. For $LaScSiH_{1.5}$, all octahedral sites are occupied by H^-; no potential electride-type material site remains in the structure.

DFT calculations clearly evidence the difference of electride-type material character between LaScSi and CeTiGe. A direct correlation with the results of NIHE experiments shows the ability of the electride-type Ru/LaScSi catalyst and the inability of the non-electride-type Ru/CeTiGe catalyst to dissociate N_2. In addition, the presence of hydride ions in the tetrahedral La_4 cavities of Ru/LaScSi catalyst leads to efficient equilibration reaction, in agreement with the calculated lowering of the Fermi level for Ru/LaScSiH compared with non-hydrogenated Ru/LaScSi. Finally, fully hydrogenated $Ru/LaScSiH_{1.5}$ is shown to lose its electride-type material's potential resulting in a low activity for N_2 activation. In these Ru/RTX compounds, the electride-type materials properties are therefore essential for the dissociation of N_2, as highlighted in Fig. 7b. However, the catalytic tests in ammonia synthesis show that under $N_2 + H_2$ mixture, the electride-type material character is not required for the catalyst to be active for NH_3 production, even if Ru/LaScSi is more active than Ru/CeTiGe, in particular above atmospheric pressure. This result suggests that the dissociation of the molecular nitrogen, as an initial step, would not be required in the case of Ru/CeTiGe. However, the presence of hydrogen in the reactant flow must be considered since it has been shown that the equilibration rate on pure Ru was increased by the addition of hydrogen [52]. The presence of H_2 in the reaction could thus have a beneficial effect for the N_2 bond cleavage. Different mechanisms can also explain the difference of

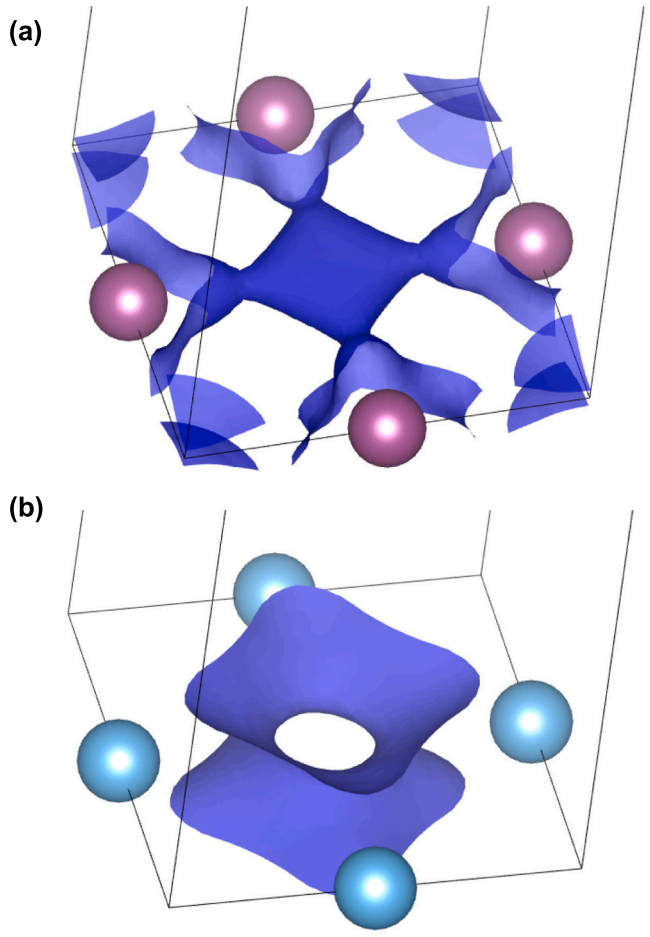

Fig. 12. Isovalue ($\rho = 2.0 \times 10^{-2}$ e$^-$.Å^{-3}) plots of the electron density in the Sc and Ti layers of (a) LaScSiH and (b) CeTiGeH based on DFT/HSE06 hybrid calculations.

Table 4
Electron populations in atomic basins in LaScSiH and CeTiGeH based on QTAIM partitioning of the valence electron density. The vacancy is located in the R_2T_4 octahedral site (R = La, Ce; T = Sc, Ti). Note that the sum of Bader populations amounts to the total number of valence electrons per formula unit (2 vacancies per f.u.).

	La/Ce	Sc/Ti	Si/Ge	H	Vacancy	Total
LaScSiH	9.46	0.91	6.41	1.63	1.18	19.00
CeTiGeH	10.38	2.73	16.20	1.69	0.00	31.00

behaviour between the two catalysts. The dissociative pathway where the N≡N bond is cleaved before any addition of hydrogen would be favoured by the electride-type material character of Ru/LaScSi, whereas Ru/CeTiGe would produce ammonia following the associative pathway in which the N≡N bond is broken upon the release of the first NH_3 [53]. The latter mechanism would not request materials having electride-type character but could be promoted by catalyst composed of hydride-containing solids. It would explain the very low activity in ammonia synthesis of $Ru_{1.3}$/GdScSi, which is unable to absorb H_2 but exhibits both the electride-type material character and a good activity for nitrogen equilibration [16].

For decades, the ammonia synthesis reaction was efficiently investigated by means of ^{15}N tracer, deuterium isotope effect, and kinetics on iron, ruthenium or nitride-based catalysts [52,54,55]. More recently, using $^{15}N_2$, the reactivity of the lattice nitrogen atoms with gas phase nitrogen was demonstrated on Co_3Mo_3N by Hunter et al. [56], raising the idea of the possible occurrence of the Mars−van Krevelen mechanism in the ammonia synthesis on nitride containing catalysts. On intermetallic-supported ruthenium catalysts investigated in the present study, the gas/solid nitrogen transfer does not occur meaning that the nitridation does not take place. Pure $^{15}N_2/^{14}N_2$ equilibration into $^{15}N^{14}N$ can then be observed and direct correlation can be done between the result of this relatively simple reaction and the capacity of the catalyst to dissociatively activate N_2, i.e. the ability of the studied catalysts for N≡N cleavage. As the equilibration activity is also dependent on the Ru particle size and morphology, this characterization technique is very useful to identify the deactivation phenomena related to the modification of the metal clusters and validate or not strategies in the design of catalysts for improvement of their durability.

4. Conclusions

Ru/LaScSi and Ru/CeTiGe catalysts were tested for the ammonia synthesis reaction at 400 °C between 1 and 5 bar of pressure. Fully hydrogenated Ru/LaScSi$H_{1.5}$ was also investigated for comparison. Both Ru/LaScSi and Ru/LaScSi$H_{1.5}$ catalysts are very active at 400 °C and have similar performances considering the difference in Ru loading. The behaviour of Ru/CeTiGe and LaScSi-based catalysts are quite close at 1 bar in terms of ammonia production rate. However, the difference of activity becomes higher at 3 and 5 bar pressure in favour of the Ru/LaScSi sample.

DFT calculations evidenced the respective electride-type vs. non-electride-type materials character of LaScSi and CeTiGe. This electride-type material character is preserved and even reinforced with hydrogen uptake in the La_4 tetrahedral cavities of the intermetallic phase. A correlation is made with the respective activity vs. inactivity for nitrogen equilibration reaction of partially hydrogenated Ru/LaScSiH_x and Ru/CeTiGeH_x. A difference of reaction pathways was proposed to link the behaviour of each sample with their activity in ammonia synthesis; a dissociative route for Ru/LaScSi and an associative pathway for Ru/CeTiGe.

CreditAuthorStatement.

Charlotte Croisé: Investigation, Visualization; **Khaled Alabd**: Investigation; **Antoine Villesuzanne**: Investigation, Conceptualization, Writing – Review and Editing; **Fabien Can**: Supervision, Funding acquisition, Project administration, Review; **Xavier Courtois**: Supervision, Funding acquisition, Review, **Etienne Gaudin**: Supervision, Writing – Review; Sophie Tencé: Supervision, Funding acquisition, Project administration, Writing - Review **Nicolas Bion**: Conceptualization, Project administration, Funding acquisition, Writing – Review & Editing.

Declaration of Competing Interest

The authors declare the following financial interests/personal relationships which may be considered as potential competing interests:

Nicolas Bion reports financial support was provided by French National Research Agency.

Data availability

Data will be made available on request.

Acknowledgments

The authors gratefully acknowledge the Région Nouvelle Aquitaine (Néo-Ammonia projet, AAPR2020-2019-8018010), the French National Agency for Research (Intermetalyst project, ANR-19-07CE-0023) and the European Regional Development Fund (ERDF) for financial support. The authors thank S. Arrii, J. Rousseau and L. Eloy for PXRD, TEM and ICP analyses respectively. This work pertains to the French government program “Investissements d’Avenir” (EUR INTREE, reference ANR-18-

EURE-0010). Computational resources were provided by the Mésocentre de Calcul Intensif Aquitain (MCIA), University of Bordeaux.

References

[1] I. Dybkjaer, Ammonia production processes, in: A. Nielsen (Ed.), Ammon. Catal. Manuf, Springer, Berlin, Heidelberg, 1995, pp. 199–327, https://doi.org/10.1007/978-3-642-79197-0_6.

[2] M. Ravi, J.W. Makepeace, Facilitating green ammonia manufacture under milder conditions: what do heterogeneous catalyst formulations have to offer? Chem. Sci. (2021) https://doi.org/10.1039/D1SC04734E.

[3] M. Capdevila-Cortada, Electrifying the Haber–Bosch, Nat. Catal. 2 (2019) 1055, https://doi.org/10.1038/s41929-019-0414-4.

[4] J.W. Makepeace, T. He, C. Weidenthaler, T.R. Jensen, F. Chang, T. Vegge, P. Ngene, Y. Kojima, P.E. de Jongh, P. Chen, W.I.F. David, Reversible ammonia-based and liquid organic hydrogen carriers for high-density hydrogen storage: recent progress, Int. J. Hydrog. Energy 44 (2019) 7746–7767, https://doi.org/10.1016/j.ijhydene.2019.01.144.

[5] M. Aziz, A.T. Wijayanta, A.B.D. Nandiyanto, Ammonia as effective hydrogen storage: a review on production, storage and utilization, Energies. 13 (2020) 3062, https://doi.org/10.3390/en13123062.

[6] B. Su, Y. Wang, Z. Xu, W. Han, H. Jin, H. Wang, Novel ways for hydrogen production based on methane steam and dry reforming integrated with carbon capture, Energy Convers. Manag. 270 (2022), 116199, https://doi.org/10.1016/j.enconman.2022.116199.

[7] S. Ghavam, M. Vahdati, I.A.G. Wilson, P. Styring, Sustainable ammonia production processes, Front. Energy Res. 9 (2021), https://doi.org/10.3389/fenrg.2021.580808 (accessed February 24, 2023).

[8] M. Fasihi, R. Weiss, J. Savolainen, C. Breyer, Global potential of green ammonia based on hybrid PV-wind power plants, Appl. Energy 294 (2021), 116170, https://doi.org/10.1016/j.apenergy.2020.116170.

[9] C. Smith, A.K. Hill, L. Torrente-Murciano, Current and future role of Haber–Bosch ammonia in a carbon-free energy landscape, Energy Environ. Sci. 13 (2020) 331–344, https://doi.org/10.1039/C9EE02873K.

[10] M. Kitano, Y. Inoue, Y. Yamazaki, F. Hayashi, S. Kanbara, S. Matsuishi, T. Yokoyama, S.-W. Kim, M. Hara, H. Hosono, Ammonia synthesis using a stable electride as an electron donor and reversible hydrogen store, Nat. Chem. 4 (2012) 934–940, https://doi.org/10.1038/nchem.1476.

[11] J.L. Dye, Electrides: early examples of quantum confinement, Acc. Chem. Res. 42 (2009) 1564–1572, https://doi.org/10.1021/ar9000857.

[12] C. Liu, S.A. Nikolaev, W. Ren, L.A. Burton, Electrides: a review, J. Mater. Chem. C 8 (2020) 10551–10567, https://doi.org/10.1039/D0TC01165G.

[13] V. Marakatti, E. Gaigneaux, Recent advances in heterogeneous catalyst for ammonia synthesis, ChemCatChem. (2020), https://doi.org/10.1002/cctc.202001141.

[14] J. Wu, Y. Gong, T. Inoshita, D.C. Fredrickson, J. Wang, Y. Lu, M. Kitano, H. Hosono, Tiered Electron anions in multiple voids of LaScSi and their applications to ammonia synthesis, Adv. Mater. 29 (2017) 1700924, https://doi.org/10.1002/adma.201700924.

[15] S. Tencé, T. Mahon, E. Gaudin, B. Chevalier, J.-L. Bobet, R. Flacau, B. Heying, U. Ch. Rodewald, R. Pöttgen, Hydrogenation studies on NdScSi and NdScGe, J. Solid State Chem. 242 (2016) 168–174, https://doi.org/10.1016/j.jssc.2016.02.017.

[16] C. Croisé, K. Alabd, S. Tencé, E. Gaudin, A. Villesuzanne, X. Courtois, N. Bion, F. Can, Influence of the rare earth (R) element in Ru-supported RScSi electride-like intermetallic catalysts for ammonia synthesis at low pressure: insight into NH3 formation mechanism, ChemCatChem. e202201172. doi:https://doi.org/10.1002/cctc.202201172.

[17] F. Brix, G. Frapper, É. Gaudry, Ammonia synthesis on the RRuSi(001) (R = Ca,La) surfaces: DFT insights revealing the active La termination of the LaRuSi electride, J. Phys. Chem. C 126 (2022) 3009–3016, https://doi.org/10.1021/acs.jpcc.1c08725.

[18] B. Chevalier, W. Hermes, E. Gaudin, R. Pöttgen, New high temperature modification of CeTiGe: structural characterization and physical properties, J. Phys. Condens. Matter 22 (2010), 146003, https://doi.org/10.1088/0953-8984/22/14/146003.

[19] J. Rodríguez-Carvajal, Recent advances in magnetic structure determination by neutron powder diffraction, Phys. B Condens. Matter 192 (1993) 55–69, https://doi.org/10.1016/0921-4526(93)90108-I.

[20] D. Martin, D. Duprez, Mobility of surface species on oxides. 1. Isotopic exchange of $^{18}O_2$ with ^{16}O of SiO_2, Al_2O_3, ZrO_2, MgO, CeO_2, and CeO_2-Al_2O_3. Activation by Noble metals. Correlation with oxide basicity, J. Phys. Chem. 100 (1996) 9429–9438, https://doi.org/10.1021/jp9531568.

[21] D. Duprez, Oxygen and hydrogen surface mobility in supported metal catalysts: study by $^{18}O/^{16}O$ and $^{2}H/^{1}H$ exchange, in: Isot. Heterog. Catal., Published by Imperial College Press and Distributed by World Scientific Publishing Co., 2006, pp. 133–181, https://doi.org/10.1142/9781860948084_0006.

[22] G. Kresse, J. Furthmüller, Efficiency of ab-initio total energy calculations for metals and semiconductors using a plane-wave basis set, Comput. Mater. Sci. 6 (1996) 15–50, https://doi.org/10.1016/0927-0256(96)00008-0.

[23] P.E. Blöchl, Projector augmented-wave method, Phys. Rev. B 50 (1994) 17953–17979, https://doi.org/10.1103/PhysRevB.50.17953.

[24] G. Kresse, J. Hafner, Ab initio molecular dynamics for liquid metals, Phys. Rev. B 47 (1993) 558–561, https://doi.org/10.1103/PhysRevB.47.558.

[25] J.P. Perdew, K. Burke, M. Ernzerhof, Generalized gradient approximation made simple, Phys. Rev. Lett. 78 (1997) 1396, https://doi.org/10.1103/PhysRevLett.78.1396.

[26] C. Loschen, J. Carrasco, K.M. Neyman, F. Illas, First-principles LDA+U and GGA+U study of cerium oxides: dependence on the effective U parameter, Phys. Rev. B 75 (2007) 035115–035122, https://doi.org/10.1103/PhysRevB.75.035115.

[27] Yue-Chao Wang, Xu Yuan-Ji, Yu Liu, Xing-Jie Han, Xie-Gang Zhu, Yi-feng Yang, Yan Bi, Hai-Feng Liu, Hai-Feng Song, First-principles study of the role of surface in the heavy-fermion compound $CeRh_2Si_2$, Phys. Rev. B 103 (2021) 165140–165148, https://doi.org/10.1103/PhysRevB.103.165140.

[28] J.L.F. Da Silva, M.V. Ganduglia-Pirovano, J. Sauer, V. Bayer, G. Kresse, Hybrid functionals applied to rare-earth oxides: the example of ceria, Phys. Rev. B 75 (2007) 045121–045131, https://doi.org/10.1103/PhysRevB.75.045121.

[29] J. Graciani, A.M. Márquez, J.J. Plata, Y. Ortega, N.C. Hernández, A. Meyer, C. M. Zicovich-Wilson, J. Fdez, Sanz, comparative study on the performance of hybrid DFT functionals in highly correlated oxides: the case of CeO_2 and Ce_2O_3, J. Chem. Theory Comput. 7 (2011) 56–65, https://doi.org/10.1021/ct100430q.

[30] S.L. Dudarev, G.A. Botton, S.Y. Savrasov, C.J. Humphreys, A.P. Sutton, Electron-energy-loss spectra and the structural stability of nickel oxide: an LSDA+U study, Phys. Rev. B 57 (1998) 1505–1509, https://doi.org/10.1103/PhysRevB.57.1505.

[31] A.V. Krukau, O.A. Vydrov, A.F. Izmaylov, G.E. Scuseria, Influence of the exchange screening parameter on the performance of screened hybrid functionals, J. Chem. Phys. 125 (2006), 224106, https://doi.org/10.1063/1.2404663.

[32] J. Heyd, G.E. Scuseria, M. Ernzerhof, Hybrid functionals based on a screened coulomb potential, J. Chem. Phys. 118 (2003) 8207–8215, https://doi.org/10.1063/1.1564060.

[33] R.F.W. Bader, A quantum theory of molecular structure and its applications, Chem. Rev. 91 (1991) 893–928, https://doi.org/10.1021/cr00005a013.

[34] G. Henkelman, A. Arnaldsson, H. Jónsson, A fast and robust algorithm for Bader decomposition of charge density, Comput. Mater. Sci. 36 (2006) 354–360, https://doi.org/10.1016/j.commatsci.2005.04.010.

[35] M. Kitano, S. Kanbara, Y. Inoue, N. Kuganathan, P.V. Sushko, T. Yokoyama, M. Hara, H. Hosono, Electride support boosts nitrogen dissociation over ruthenium catalyst and shifts the bottleneck in ammonia synthesis, Nat. Commun. 6 (2015) 6731, https://doi.org/10.1038/ncomms7731.

[36] S.G. Dale, A. Otero-de-la-Roza, E.R. Johnson, Density-functional description of electrides, Phys. Chem. Chem. Phys. 16 (2014) 14584–14593, https://doi.org/10.1039/c3cp55533j.

[37] L.A. Burton, F. Ricci, W. Chen, G.-M. Rignanese, G. Hautier, High-throughput identification of electrides from all known inorganic materials, Chem. Mater. 30 (2018) 7521–7526, https://doi.org/10.1021/acs.chemmater.8b02526.

[38] O. El Bakouri, V. Postils, M. Garcia-Borras, M. Duran, J.M. Luis, S. Calvello, A. Soncini, E. Matito, F. Feixas, M. Sola, Metal cluster electrides: a new type of molecular electride with delocalised polyattractor character, Chem. Eur. J. 24 (2018) 9853–9859, https://doi.org/10.1002/chem.201800878.

[39] V. Postils, M. Garcia-Borras, M. Sola, J.M. Luis, E. Matito, On the existence and characterization of molecular electrides, Chem. Commun. 51 (2015) 4865–4868, https://doi.org/10.1039/c5cc00215j.

[40] J. Wang, Q. Zhu, Z. Wang, H. Hosono, Ternary inorganic electrides with mixed bonding, Phys. Rev. B 99 (2019), 064104, https://doi.org/10.1103/PhysRevB.99.064104.

[41] Q. Zhu, T. Frolov, K. Choudhary, Computational discovery of inorganic Electrides from an automated screening, Matter. 1 (2019) 1293–1303, https://doi.org/10.1016/j.matt.2019.06.017.

[42] M. Miao, R. Hoffmann, High-pressure electrides: the chemical nature of interstitial quasiatoms, J. Am. Chem. Soc. 137 (2015) 3631–3637, https://doi.org/10.1021/jacs.5b00242.

[43] K. Momma, F. Izumi, VESTA 3 for three-dimensional visualization of crystal, volumetric and morphology data, J. Appl. Crystallogr. 44 (2011) 1272–1276, https://doi.org/10.1107/S0021889811038970.

[44] C. Ritter, A. Provino, P. Manfrinetti, A.K. Pathak, Tetragonal to triclinic structural transition in the prototypical CeScSi induced by a two-step magnetic ordering: a temperature-dependent neutron diffraction study of CeScSi, CeScGe and LaScSi, J. Phys. Condens. Matter 29 (2016), 045802, https://doi.org/10.1088/1361-648X/29/4/045802.

[45] B. Chevalier, W. Hermes, B. Heying, U.Ch. Rodewald, A. Hammerschmidt, S. F. Matar, E. Gaudin, R. Pöttgen, New hydrides REScSiH and REScGeH (RE = La, Ce): structure, magnetism, and chemical bonding, Chem. Mater. 22 (2010) 5013–5021, https://doi.org/10.1021/cm101290f.

[46] T. Mahon, E. Gaudin, A. Villesuzanne, R. Decourt, J.-L. Bobet, O. Isnard, B. Chevalier, S. Tencé, Hydrogen insertion in the intermetallic GdScGe: a drastic reduction of the dimensionality of the magnetic and transport properties, Inorg. Chem. 57 (2018) 14230–14239, https://doi.org/10.1021/acs.inorgchem.8b02247.

[47] T. Mahon, S. Tencé, R. Pöttgen, B. Chevalier, E. Gaudin, Study of the structural transition and hydrogenation of CeTiGe, J. Alloys Compd. 805 (2019) 701–708, https://doi.org/10.1016/j.jallcom.2019.07.104.

[48] Y. Ogata, K. Aika, T. Onishi, Isotopic equilibration reaction of dinitrogen over raney ruthenium with and without potassium, Chem. Lett. 13 (1984) 825–828, https://doi.org/10.1246/cl.1984.825.

[49] O. Hinrichsen, F. Rosowski, A. Hornung, M. Muhler, G. Ertl, The kinetics of Ammonia synthesis over Ru-based catalysts: 1. The dissociative chemisorption and associative desorption of N2, J. Catal. 165 (1997) 33–44, https://doi.org/10.1006/jcat.1997.1447.

[50] A.A. Dyachenko, A.V. Lukoyanov, V.I. Anisimov, A.R. Oganov, Electride properties of ternary silicide and germanide of La and Ce, Phys. Rev. B 105 (2022), 085146, https://doi.org/10.1103/PhysRevB.105.085146.

[51] T. Mahon, E. Gaudin, A. Villesuzanne, B. Chevalier, S. Tencé, Effect of carbon insertion on the structural and magnetic properties of NdScSi, Inorg. Chem. 58 (2019) 15255–15268, https://doi.org/10.1021/acs.inorgchem.9b02260.
[52] K. Urabe, K.-I. Aika, A. Ozaki, Activation of nitrogen by alkali metal-promoted transition metal: VI. Hydrogen effect on isotopic equilibration of nitrogen and rate-determining step of ammonia synthesis on potassium-promoted ruthenium catalysts, J. Catal. 42 (1976) 197–204, https://doi.org/10.1016/0021-9517(76)90253-0.
[53] Q. Wang, J. Guo, P. Chen, Recent progress towards mild-condition ammonia synthesis, J. Energy Chem. 36 (2019) 25–36, https://doi.org/10.1016/j.jechem.2019.01.027.
[54] K. Aika, A. Ozaki, Mechanism and isotope effect in ammonia synthesis over molybdenum nitride, J. Catal. 14 (1969) 311–321, https://doi.org/10.1016/0021-9517(69)90321-2.
[55] K.-I. Aika, A. Ozaki, Kinetics and isotope effect of ammonia synthesis over a singly-promoted iron catalyst, J. Catal. 19 (1970) 350–352, https://doi.org/10.1016/0021-9517(70)90257-5.
[56] S.M. Hunter, D.H. Gregory, J.S.J. Hargreaves, M. Richard, D. Duprez, N. Bion, A study of N-15/N-14 isotopic exchange over cobalt molybdenum nitrides, ACS Catal. 3 (2013) 1719–1725, https://doi.org/10.1021/cs400336z.